Inertia and diffusion effects on reactive transport with fluid-solid reactions in rough fracture flows

Woonghee Lee, Seonkyoo Yoon, and Peter K. Kang

Phys. Rev. Fluids **8**, 054502 — Published 25 May 2023

DOI: 10.1103/PhysRevFluids.8.054502

Inertia and Diffusion Effects on Reactive Transport with Fluid–Solid Reactions in Rough Fracture Flows

Woonghee Lee,[1, 2] Seonkyoo Yoon,[1] and Peter K. Kang[1, 2, *]
[1] *Department of Earth and Environmental Sciences,*
University of Minnesota, Minneapolis, MN 55455, USA
[2] *Saint Anthony Falls Laboratory, University of Minnesota, Minneapolis, MN 55414, USA*

(Dated: April 28, 2023)

Fluid inertia is known to exert a dominant control over transport processes in fracture flows. In particular, recirculating flows readily arise in inertial rough fracture flows and have been shown to cause anomalous transport by trapping particles. However, the combined effects of fluid inertia and solute diffusion on reactive transport involving fluid–solid reactions have thus far been elusive. This study investigates reactive transport involving an irreversible fluid–solid bimolecular reaction for wide ranges of Reynolds (Re) and Péclet (Pe) numbers and elucidates how the interplay between inertia and diffusion effects controls the dynamics of reactive transport. Solute diffusion (Pe) controls mainly the total reaction amount, whereas fluid inertia (Re) governs the reaction dynamics by inducing complex flow structures such as flow channeling and recirculating flows. Specifically, recirculating flows are shown to facilitate fluid-solid reactions by increasing the residence time of particles near the fluid-solid interfaces, and such trapping effects increase as Pe increases. Further, flow channeling and recirculating flows exert dominant control over the transport of both reactants and products. We elucidate the reactive transport dynamics by analyzing particle trajectories and quantifying Lagrangian velocity statistics and reaction-related measures. Based on the improved understanding, we then propose an upscaled reactive transport model that incorporates Lagrangian velocity statistics and velocity-dependent reaction probability, and show that the upscaled model successfully captures reactive transport over wide ranges of Re and Pe.

I. INTRODUCTION

The reactions between dissolved reactants in the fluid phase and mineral components in the solid phase in fracture flows govern many subsurface processes and applications such as groundwater contamination and remediation, geothermal energy extraction, nuclear waste disposal, geologic carbon sequestration, karst formation, and global biogeochemical cycling [1–15]. Surface reactions in channel flows also govern many hydrologic processes and engineering applications such as hyporheic flow, microfluidic mixers, water filtration technologies, fuel cells, and catalytic reactors [16–27].

In such contexts, reactive transport dynamics can vary widely depending not only on the structural heterogeneity of channel geometry, but also on inertia and diffusion regimes. Recent studies indeed have shown that the interplay between fluid inertia and reactant diffusion is a key controlling factor for reactive transport in rough fracture flows [28–32]. More specifically, fluid inertia can induce complex flow structures, such as flow channeling and recirculating flows, in rough fracture flows [32–37]. These flow structures govern the advective transport of reactants. On the other hand, the diffusion of reactants leads to mixing and chemical reactions. Therefore, the respective roles of inertia and diffusion effects on reaction dynamics should be properly understood to accurately predict reactive transport in fracture flows.

The effects of fluid inertia and solute diffusion on conservative solute transport in rough fracture flows have been widely investigated [33–36, 38–44]. Previous studies have shown that recirculating flows developed at inertial flow regimes can induce non-Fickian (anomalous) transport, manifested as both the anomalously early arrival and late-time tailing of tracers compared to those in Fickian transport [33–36, 38]. For example, recirculating flows increase flow channeling by narrowing the effective aperture of a fracture, thereby inducing early arrivals of solutes at downstream locations. On the other hand, recirculating flows induce late arrivals of solutes by increasing the solute residence time via a trapping effect, where the degree of the trapping effect has been demonstrated to be highly sensitive to solute diffusivity [38].

Recent studies have also shown the strong effects of recirculating flows and solute diffusion on reactive transport in fracture flows. For example, Lee and Kang [45] and Yoon and Kang [46] revealed that the increased residence time of reactants in recirculating flows causes mixing-induced fluid-fluid reaction hot spots in channel flows. With regard to fluid-solid reactions, Deng *et al.* [30] discussed the potential effects of recirculating flows' trapping effect on

---

[*] pkkang@umn.edu

fluid-solid reactions, and Zhou *et al.* [47] showed the effects of recirculating flows on the effective dissolution rates and channel dissolution patterns. Sund *et al.* [48] and Sherman *et al.* [49] focused more on investigating the trapping effect of recirculating flows on the transport of solutes with bimolecular fluid-solid reactions, such as removal of reactants at the reaction location or adsorbing/desorbing processes in idealized sinusoidal channels. However, the studies are limited to relatively low Reynolds number regimes (Re $< O(1)$) [48, 49], although inertia effects can vary considerably in fracture flows. Further, we currently lack a comprehensive understanding of the effects of fluid inertia and solute diffusion on reactive transport with surface reactions. Although it is known that inertia and diffusion effects can vary widely in rough fracture flows, their compounding effects on reactive transport involving fluid–solid reactions have thus far remained elusive.

To improve the fundamental understanding of reactive transport involving fluid–solid reactions in rough fracture flows, we study such transport over wide ranges of inertia and diffusion regimes. We consider a simple instantaneous bimolecular fluid–solid reaction, $A + Solid \to C$, where A converts to C via a surface reaction. The use of such a simple reaction allows us to focus on the effects of inertia and diffusion on the reactive transport dynamics. We then systematically explore wide ranges of inertia and diffusion regimes using Lagrangian-based reactive transport simulations and elucidate the respective role of inertia and diffusion on the fluid-solid reactive transport dynamics. Based on the improved understanding, we also propose an upscaled reactive transport model with fluid-solid reactions by incorporating the velocity-dependent reaction probability into the spatial Markov model. The velocity-dependent reaction rule effectively captures the inertia and diffusion effects on the fluid-solid reactions, and the proposed upscaled model successfully captured the full reactive transport dynamics, including reactants and products. To the best of our knowledge, this is the first study that successfully captures both reactants and products from the fluid-solid reactions using a continuous time random walk (CTRW) framework.

This paper is structured as follows. In Section II, we present methods for rough fracture generation, fluid flow, and reactive transport simulations. In Section III, we discuss the key characteristics of fluid flow and fluid–solid reaction dynamics in rough fracture flows. In Section IV, we analyze Lagrangian velocity statistics and characterize reaction probability in terms of the Lagrangian velocity statistics. Based on these, we then propose an upscaled modeling framework that is efficiently parameterized as a function of Lagrangian velocity statistics. Finally, in Section V, we present the conclusion of the study.

II. SIMULATION METHODS

A. Generation of Rough Fractures

To study reactive transport in rough fracture flows, we first generate an ensemble of self-affine profiles, which are often observed in nature [50–52]. The self-affine profiles are scale-invariant, such that the standard deviation of the height difference Δz between two points separated by lateral distance Δx can be expressed as

$$\sigma_{\Delta z}(\Delta x) = \lambda^{-H} \sigma_{\Delta z}(\lambda \Delta x), \tag{1}$$

where λ is the scaling factor, and H is the Hurst exponent that determines the surface roughness. We consider the Hurst exponent $H = 0.7$ which is a commonly observed value in nature [2, 53, 54]. Note that the surface profile is flat for $H = 1$ and becomes rougher as the value of H decreases. We generate 2D fracture geometries as shown in Fig. 1 (a), using the successive random addition algorithm [55, 56]. Note that the channel flows are often simplified as 2D as considered in this study, but the 3D flow effects can potentially be important in fluid-solid reactions [35, 45]. Understanding 3D flow effects on reactive transport with surface reactions should be the topic of future study. The longitudinal length of the fracture is $100a$, where a is the aperture. We generate an ensemble of ten rough fracture realizations with the same length, aperture, and the roughness parameter $H = 0.7$.

B. Flow Simulations

We simulate fluid flow through the generated rough fractures by solving the steady-state incompressible Navier–Stokes equations (Eq. (2)) and the continuity equation (Eq. (3)) using the finite volume method [57]:

$$\vec{u} \cdot \nabla \vec{u} = -\frac{1}{\rho} \nabla p + \nu \nabla^2 \vec{u}, \tag{2}$$

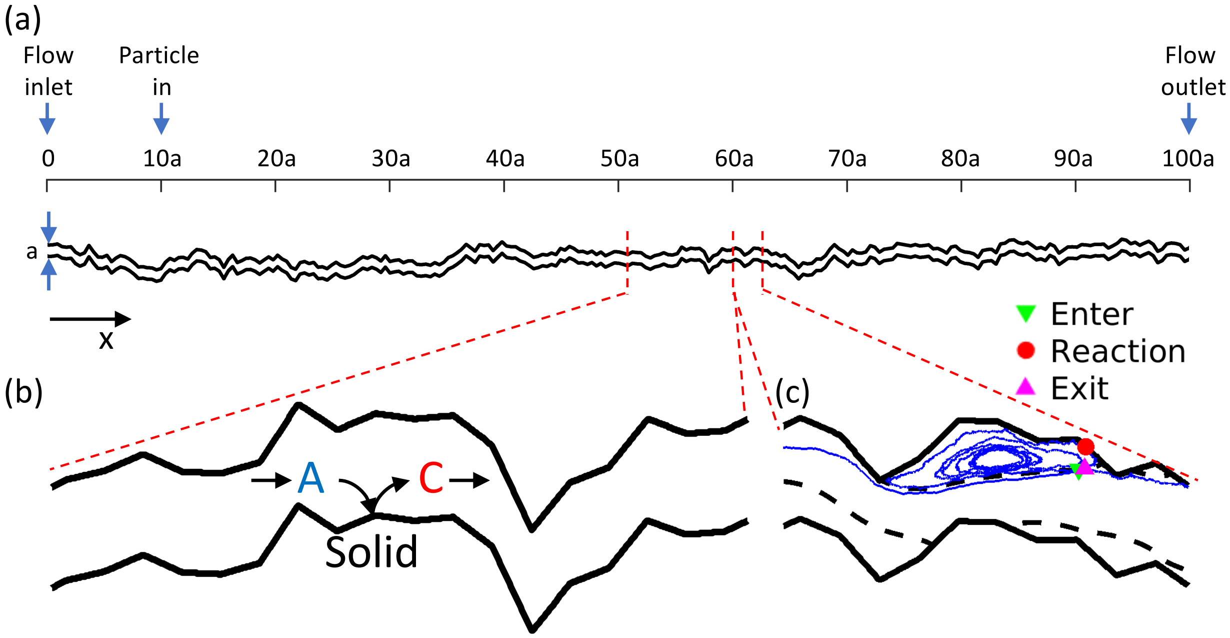

FIG. 1. (a) Example of rough fracture geometry, with aperture a and fracture length $100a$. Vertical arrows show the inlet and outlet of fluid and the injection location of solute particles. Particles are injected at $x = 10a$. (b) Schematic of fluid–solid bimolecular reaction process. C particles are released when A particles react with solid surfaces. (c) Trajectory of A particle that reacts in recirculation zone at Re = 1 and Pe = 10^3. Locations of entrance (green downward triangle), reaction (red dot), and exit (magenta upward triangle) in recirculation zone are indicated.

$$\nabla \cdot \vec{u} = 0, \tag{3}$$

where t is the time, $\vec{u}$ is the fluid velocity, p is the pressure, ν is the fluid kinematic viscosity, and ρ is the fluid density. We set a constant flux condition on the fluid inlet boundary and a zero-gradient pressure condition on the fluid outlet boundary (Fig. 1 (a)). At the fracture walls, the no-slip boundary condition is imposed. We quantify the fluid inertia effect using Reynolds number (Re), defined as:

$$\mathrm{Re} = \frac{\bar{u}a}{\nu}, \tag{4}$$

where $\bar{u}$ is the mean fluid velocity. We solve the flow equations at Re = [1, 10, 20, 40, 60, 80, 100] to encompass a wide range of steady inertia flow regimes [44]. The discretization of fracture domains is 10,000 grid cells in the x-direction and 100 grid cells in the y-direction; thereby, a single-cell size is $a/100 \times a/100$. We confirmed that flow fields with a finer discretization exhibit negligible difference.

C. Reactive Transport Simulations with Surface Reactions

We quantify the diffusion effect using the Péclet number (Pe), defined as

$$\mathrm{Pe} = \frac{\bar{u}a}{D}. \tag{5}$$

We consider Pe = [10^2, 10^3, 10^4] to investigate a wide range of diffusion regimes. In this study, we vary Re and Pe values independently by adjusting the fluid kinematic viscosity, ν, and the molecular diffusivity, D, to discern the respective roles of inertia and diffusion on the dynamics of reactive transport. A similar approach was recently used to elucidate inertia and diffusion effects on conservative and mixing-induced reactive transport [32, 38, 46, 58].

The ranges of Re $= [1 - 100]$ and Pe $= [10^2 - 10^4]$ are in the observable range of Schmidt number, Sc $=$ Pe/Re, which represents various combinations of fluids and solutes under various thermodynamic conditions [59–61]. To avoid case-specific results, we consider ten rough fracture realizations with the length of $100a$ and the aperture of a for each combination of Re and Pe. In total, we run $10^{(H)} \times 7^{(Re)} \times 3^{(Pe)} = 210$ reactive transport simulations.

For surface reactions, we consider an irreversible fluid–solid bimolecular reaction as follows:

$$A_{(aq)} + Solid \rightarrow C_{(aq)}. \tag{6}$$

The reactant species, A, and product species, C, are dissolved chemical species in the fluid phase. On the other hand, *Solid* represents a reactive mineral species that is assumed to be sufficient and evenly distributed on the fracture surfaces such that the reactivity is constant across the solid boundaries and over time. We also assume that the aperture evolution is negligible during the reactive transport simulations. This allows us to simplify the modeling approaches and also to focus on the role of flow fields on reactive transport dynamics. The effects of aperture evolution due to dissolution on reactive transport should be a topic of future research. The reaction between the chemical species A and the solid surfaces releases the chemical species C as a passive solute into the fluid, as schematically shown in Fig. 1 (b). Similar setups of the bimolecular fluid-solid reactions have been used in previous studies to understand reactive transport processes in channel and porous media flows [48, 49, 62–64]. However, the previous studies are limited to relatively narrow Peclet and Reynolds number regimes (Re $< O(1)$), and did not track the product particle. It is important to track both reactant and product species under wide ranges of mass diffusion and fluid inertia regimes in subsurface processes. For example, in the carbon mineralization process, dissolution of mafic and ultramafic rocks by CO_2-dissolved acidic fluid releases cations, such as calcium and magnesium, into the fluid; then, the cations react with CO_2 and form stable carbonate minerals [65, 66]. Therefore, the fluid-solid reaction, such as mineral dissolution, is a critical step in the carbon mineralization process, and understanding the respective transport of reactant and product ions under various mass diffusion and fluid flow conditions is essential to understand the carbon mineralization process rigorously. In addition to that, the simple fluid–solid reaction can be considered as a building block of more complex reactions such as mineral dissolution and precipitation [30, 63, 64, 67–70], fate of contaminated water [71, 72], metabolic activity in biofilms [14], water filtration and purification [20–23], and catalytic surface reactions [26, 27].

Reactive transport involving the fluid–solid reaction is described using the advection–diffusion equation with reactive boundary conditions [49, 73, 74] as follows:

$$\frac{\partial C_i(\mathbf{x},t)}{\partial t} + \nabla \cdot [\vec{u}(\mathbf{x}) C_i(\mathbf{x},t)] = \nabla \cdot [D \nabla C_i(\mathbf{x},t)] \quad i = A \;\&\; C \quad \forall\, \mathbf{x} \in \Gamma_{\text{fluid}}, \tag{7a}$$

$$\frac{\partial C_A(\mathbf{x},t)}{\partial t} = -D\frac{\partial C_A}{\partial n} \quad \forall\, \mathbf{x} \in \Gamma_{\text{surface}}, \tag{7b}$$

$$\frac{\partial C_C(\mathbf{x},t)}{\partial t} = D\frac{\partial C_A}{\partial n} \quad \forall\, \mathbf{x} \in \Gamma_{\text{surface}}, \tag{7c}$$

where $C_A(\mathbf{x},t)$ and $C_C(\mathbf{x},t)$ are the reactant and product concentration fields, respectively, at time t. Moreover, D is the molecular diffusivity, and n is the normal vector pointing toward the fluid from the fracture surfaces. The advection–diffusion equation (Eq. (7a)) governs the transport of A and C in the fluid phase, whereas the reactive boundary conditions (Eqs. (7b) and (7c)) determine the fluid–solid reaction at the fracture surfaces. We consider a catalytic reaction such that the A particles that diffuse toward the surfaces instantaneously convert into the C particles at the contact locations between the A particles and the surfaces. In such a reaction system, the reaction rate is directly determined by the diffusive flux toward the fracture surfaces [75–80]. The simplicity of this catalytic reaction allows us to focus on the role of transport-limited, specifically diffusion-limited, reaction on the fluid–solid reactive transport dynamics [62]. Fig. 1 (c) shows an example of a particle trajectory where an A particle enters a recirculating flow, is converted into a C particle by the collision with the surface, and exits from the recirculating flow.

To numerically solve Eq. (7), we use a Lagrangian method [81–83]. The Lagrangian approach can simulate solute transport without numerical dispersion, allowing particle motions to be accurately captured even at high-Pe regimes [81, 82]. The particle motion is described by the discretized Langevin equation [84]:

$$\mathbf{x}(t + \Delta t) = \mathbf{x}(t) + \vec{u}(\mathbf{x}(t))\Delta t + \sqrt{2D\Delta t}\,\eta(t), \tag{8}$$

where $\mathbf{x}(t)$ is a particle trajectory, Δt is a time step, and $\eta(t)$ represents independent and identically distributed Gaussian variables with zero mean and unit variance. For each simulation, we inject 5×10^4 A particles as a flux-weighted line injection at the downstream location of $x = 10a$ (Fig. 1 (a)). At each time step Δt, the A particles first move via advective particle motion, followed by a diffusion step. The advective step is solved using a streamline-based particle tracking algorithm that honors no-slip boundary conditions [81, 82]. To determine the time step Δt for each particle movement, we compute characteristic advection and diffusion times; then, we choose the smaller between the two. Thus, the time step is not fixed and dynamic. The characteristic advection time, Δt_{adv}, is defined as a time for a particle to travel to a grid cell boundary from its position by advection [82], and the characteristic diffusion time step is defined as $\Delta t_{\mathrm{diff}} = (dx/10)^2/Dm$. Here, dx is the grid cell size, and Dm is the molecular diffusion coefficient. Thus, Δt_{diff} is the characteristic time required for a solute particle to move a tenth of the grid cell size by diffusion, which is a strong constraint to avoid any numerical artifacts. Additionally, the size of the time step (Δt) used in the simulation could affect the outcomes [85, 86]. To address this issue, we conducted tests using smaller time steps ($\Delta t/2$ and $\Delta t/4$) and observed that the essential simulation results remain consistent and independent of the time step. However, to gain a deeper understanding of the impact of the time step on the particle-tracking algorithm for a bimolecular fluid-solid reaction, further theoretical analysis is necessary in future research [85, 86]. We consider a reflection boundary condition when the particles encounter the fracture walls during the diffusion step [49, 58, 87]. If an A particle collides with fracture surface, the A particle converts into a C particle at the collision location. The C particle gets released into the fluid phase via the reflection boundary condition, and the C particle continues to be transported without further reactions. Movies showing examples of the reactive transport simulations can be found in the supplementary material [88].

III. SIMULATION RESULTS AND ANALYSIS

A. Inertia Effects on Flow Properties

Transport and reaction processes in rough fracture flows are fundamentally controlled by the underlying flow fields [38, 45, 58]. Thus, we first analyze the flow properties at different Re values to quantify the inertia effects on fluid flow. Figs. 2 (a) and (b) show the normalized velocity fields with streamlines at Re = 1 and 100. The color bar shows the normalized velocity magnitudes, where the normalization is based on the maximum velocity magnitude for a given case. In contrast to the Re = 1 case, significant recirculation zones are observed at Re = 100 (Fig. 2 (b)). The recirculating flows, induced by the interplay between fluid inertia and rough surfaces, reduces the effective aperture, thereby also enhancing the flow focusing (channeling) along the center of the fracture.

We delineate recirculation zones using the zero-integral-flux method [89] and quantify the area of the recirculation zones at each Re case. Figs. 2 (c) and (d) show the delineated recirculation zones in gray and the main flow channels in white at Re = 1 and 100. We then calculate the ratio of the recirculation area over the entire domain area for the ensemble of 10 realizations. As shown in Fig. 2 (e), the ratio of the recirculation area is negligible up to Re = 20 but then increases up to approximately 23 % at Re = 100. The increasing trend is approximately linear from Re = 20 to Re = 100.

We further quantify the inertia effects on the flow fields by plotting the probability density functions (PDFs) of the Eulerian velocity magnitudes. Fig. 3 shows the PDFs of the velocity magnitudes in the entire domain, main flow channel, and recirculation zones at Re = 1 and 100. The recirculation zones led to the noticeable differences between the velocity PDFs for Re = 1 and 100 (blue circles and red triangles, respectively). First, the effects of strong recirculating flows at Re = 100 are evident in the slow velocities. As shown in Fig. 3 (a), the probabilities of slow velocities (velocity magnitudes smaller than 10^{-2} m/s, the vertical dashed line) are noticeably higher at Re = 100 (solid red line with triangles) than at Re = 1 (solid blue line with circles). This is because the recirculation zones consist of slow velocities, as shown by the yellow line with triangles in Fig. 3 (a). This implies that the recirculation zones will act as trapping zones where particles are kept near the fracture surfaces for an extended time, as evidenced by the particle trajectory in Fig. 1 (c).

The enhanced flow channeling at Re = 100 is evident from Fig. 3 (b). The velocity PDFs of the main channel at Re = 100 (solid red line with triangles) and Re = 1 (solid blue line with circles) have a similar shape, but the Re = 100 case shows a higher probability for higher velocity magnitudes (velocity magnitudes greater than 10^{-2} m/s, the vertical dashed line). This is because the recirculating flows increase the velocities in the main flow channel by decreasing the effective aperture. The strong flow channeling will cause the particles to travel through the fracture faster, which may inhibit fluid–solid reactions because the channeling will inhibit particles from reaching the fracture walls. On the other hand, the flow channeling will increase the spreading of reactants, which may contribute to fluid–solid reactions. We investigate the effects of the aforementioned flow properties on transport and reaction dynamics in the following subsections.

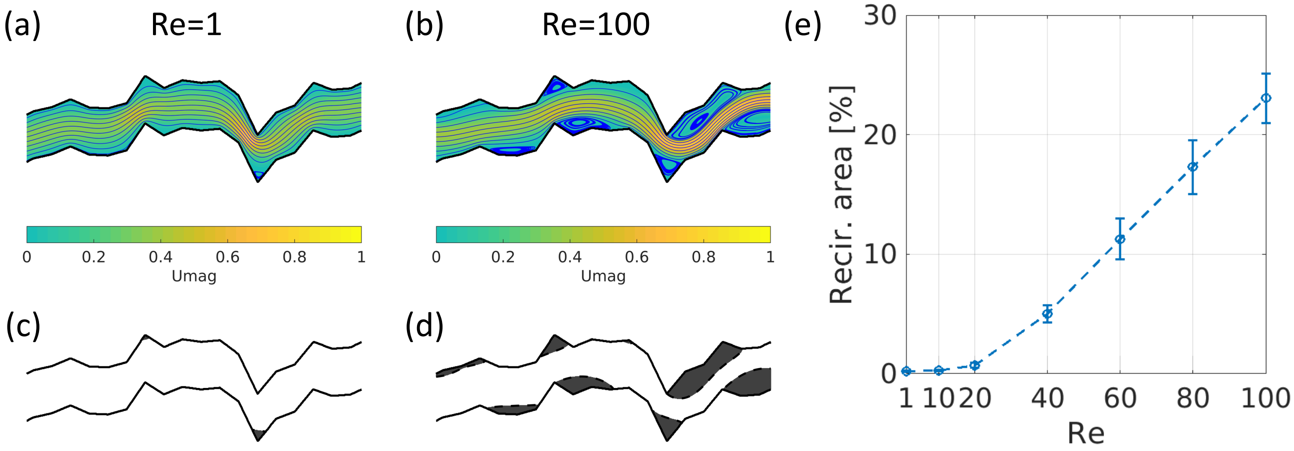

FIG. 2. (a–b) Normalized Eulerian velocity magnitude fields at Re = 1 and 100 with streamlines. Velocity magnitudes are normalized based on maximum velocity for a given case. (c–d) Delineated recirculation zones in gray and main flow channels in white. (e) Ratio of recirculation area over entire domain area as function of Re. Circles and error bars show mean and standard deviation, respectively, of 10 realizations.

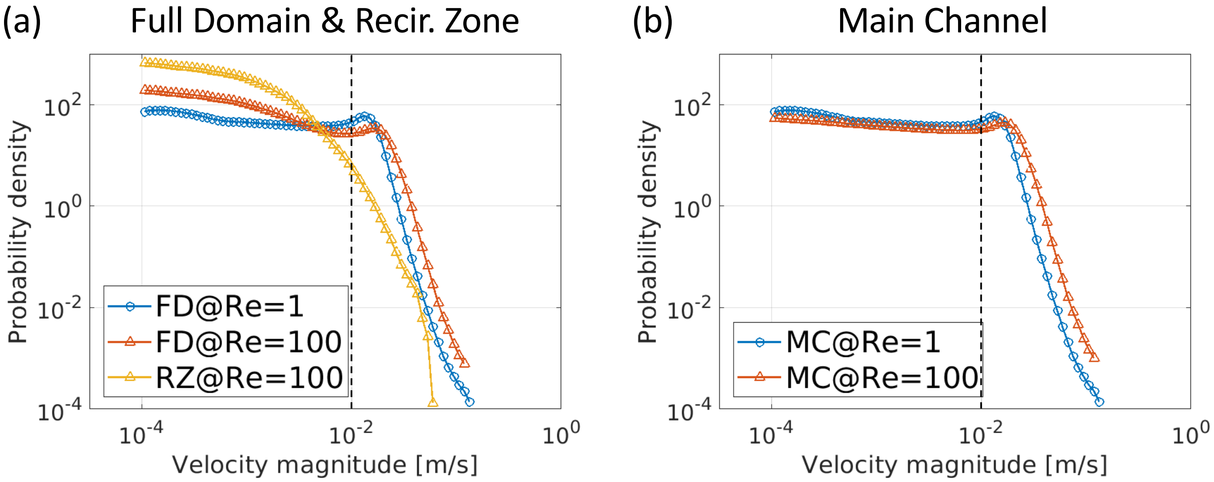

FIG. 3. Probability density functions (PDFs) of Eulerian velocity magnitudes from (a) full domain (FD) at Re = 1 (solid blue line with circles) and Re = 100 (solid red line with triangles), and recirculation zones (RZ) at Re = 100 (solid yellow line with triangles). (b) Velocity PDFs of main flow channel (MC) at Re = 1 (solid blue line with circles) and Re = 100 (solid red line with triangles). Note that "full domain" refers to the entire domain, including the main flow channel (white area in Figs. 2 (c) and (d)) and recirculation zones (gray area in Figs. 2 (c) and (d)). The vertical dashed lines indicate the location of 10^{-2} m/s on the x-axis. Eulerian velocity magnitudes are obtained from ensemble of 10 realizations.

B. Inertia and Diffusion Effects on Reactive Transport

1. *First-passage Time Distributions*

Herein, we present and discuss the first-passage time distributions (FPTDs), also known as breakthrough curves, for each combination of Re = [1, 100] and Pe = $[10^2, 10^3, 10^4]$. We examine both conservative tracer scenarios and reactive tracer scenarios, in which we inject 5×10^4 particles for each simulation. In the conservative scenario, we inject passive tracers that do not undergo any reactions. The comparison of FPTDs obtained from the conservative and reactive transport simulations is helpful for understanding both the transport and reaction dynamics. Fig. 4 shows the FPTDs at $x = 90a$ for the conservative scenario (blue lines) and for the reactive scenario (red lines showing the FPTDs of reaction-product C particles). Because both the reactant A particles and the product C particles behave as passive tracers in the fluid phase, we can view the product C particles as a subset of the conservative particles. Fig. 4 (a) shows the FPTDs for the conservative scenario and of the C particles at two different Re values, where Pe/Re is fixed to 100. The other figures show the FPTDs at two different Re values but with fixed Pe values of 10^2, 10^3, and 10^4.

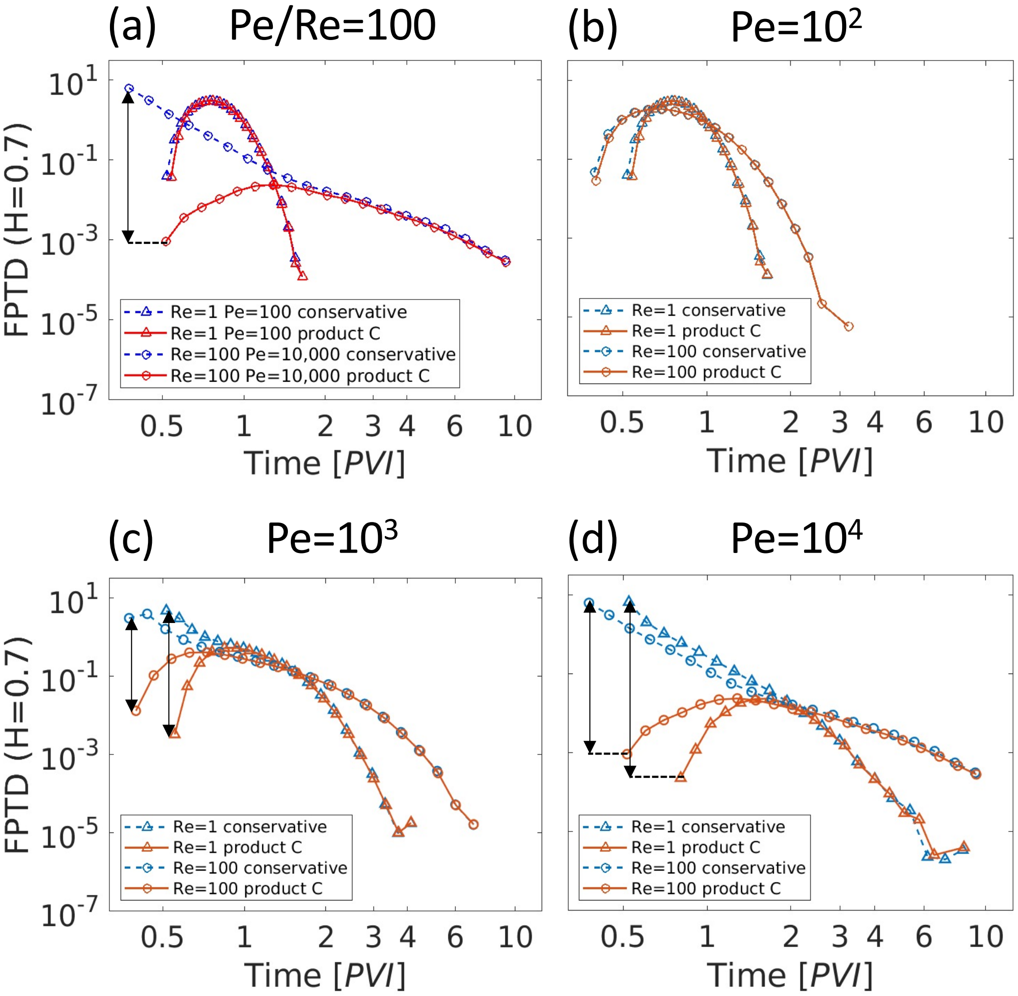

FIG. 4. First-passage time distributions (FPTDs) at $x = 90a$. Herein, y-axis is normalized based on total number of injected particles, whereas x-axis is normalized based on one pore volume injection (1 PVI), i.e., time required to inject fluid volume equal to that of the fracture domain. (a) Solid red lines indicate FPTDs of conservative-scenario particles (conservative transport), whereas dashed blue lines indicate FPTDs of product C particles (reactive transport) in cases wherein Re and Pe increase proportionally (Pe/Re = 100). Re = 1 & Pe = 10^2 (triangle marks) and Re = 100 & Pe = 10^4 (circle marks). (b)–(d) Solid orange lines indicate FPTDs of conservative-scenario particles (conservative transport), whereas dashed sky-blue lines indicate FPTDs of product C particles (reactive transport) at Re = 1 (triangle marks) and 100 (circle marks) for Pe = $[10^2, 10^3, 10^4]$.

First, increase in the Re and Pe significantly increases the overall spreading. For both the conservative-scenario particles and reaction products, the early arrival and late-time tailing in the FPTDs intensify as the Re and Pe increases (Fig. 4 (a)). To elucidate the effects of inertia, we compare FPTDs at two different Re values but with fixed Pe (Figs. 4 (b–d)). The increase in Re clearly leads to enhanced spreading. Early arrival and late tailing are the two key features of non-Fickian transport, and the role of recirculating flows in inducing such anomalous transport in rough fracture has been demonstrated [33–35, 38, 58, 90, 91]. This study shows that the inertia effect also exerts a dominant control over reactive transport with heterogeneous reactions. As discussed in the previous section, an increase in Re develops recirculating flows, and recirculating flows enhance the flow channeling. Therefore, as Re increases, both the conservative and product C particles can arrive earlier through the fast main flow channels and also arrive later because of the trapping effect of the recirculating flows.

Second, in general, there are large differences between the conservative and product C particles in the early-arrival regimes, whereas those in the late-arrival regimes are almost identical. The double-headed arrows in Fig. 4 indicate the differences in the early arrivals, and these differences magnify as both Re and Pe increase. The difference is not noticeable at Pe = 10^2 (Fig. 4 (b)) but becomes significant as Pe increases (Fig. 4 (c) and (d)). This is mainly due to the natures of the fluid–solid reaction and the diffusion effect. The A particles that stay near the fracture walls have higher chances to undergo reactions compared to the A particles that stay near the channel center. Therefore, the reaction probability is larger for the particles with larger arrival times, leading to a similar tailing behavior between the conservative-scenario particles and product C. On the other hand, the A particles that stay near the channel center tend not to undergo the reaction, leading to significant differences in the early arrivals. Such effect diminishes as the diffusion effect increases because the increase in diffusion allows particles to easily travel across in the fracture-width direction.

Fig. 5 (a) shows the ratio of the number of product C particles to the number of injected A particles at the breakthrough location $x = 90a$ as a function of Pe for both Re = 1 and 100. When the ratio is one, it indicates that all the injected particles underwent the reaction. The figure shows that Pe is the primary control on the overall reaction amount. At Pe = 10^2, most A particles undergo reactions because of the enhanced diffusion, leading to the identical FPTDs between the conservative-scenario particles and product C particles (Fig. 4 (b)). To quantify the inertia effect on the overall reaction amount, we estimated the percentage change in the number of the C particles between the Re = 100 and Re = 1 cases $((\sum \mathrm{Nc}_{@\mathrm{Re}=100} - \sum \mathrm{Nc}_{@\mathrm{Re}=1}) / \sum \mathrm{Nc}_{@\mathrm{Re}=1})$ at fixed Pe values. As shown in Fig. 5 (b), the percentage increases as Pe increases (0.3% at Pe = 10^2, 8% at Pe = 10^3, and 75% at Pe = 10^4). This indicates that the recirculation zones facilitate the fluid–solid reactions and that this effect increases as Pe increases. The 2D recirculation zones are advectively disconnected from the main flow channel [33, 34], and the recirculating flows could act as reaction barriers for fluid–solid reactions [30]. However, for the transport-limited reaction considered in this study, once the particles enter the recirculation zones via diffusion, the trapped particles have a significantly higher chance to undergo reactions. In 3D, recirculation zones and main flow channel are connected through advective flow paths and such connectivity can strongly affect mixing and transport [35, 45]. Such 3D recirculating flow features would have a potential influence on surface reactions. Therefore, the effects of 3D recirculating flows on fluid-solid reaction requires a future work.

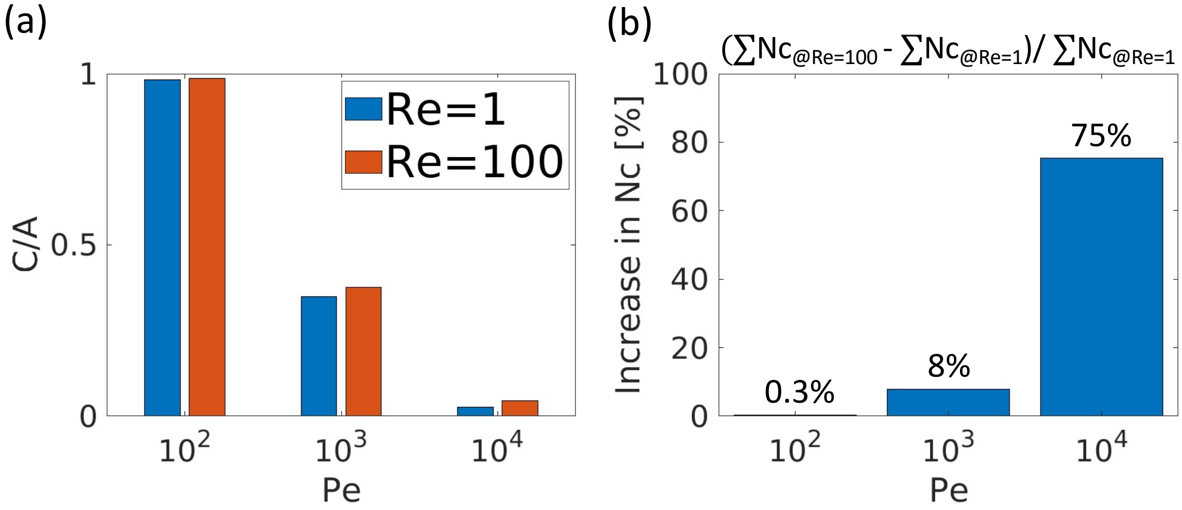

FIG. 5. (a) Mass ratio of product C particles to injected A particles estimated at breakthrough location $x = 90a$ for Re = 1 (blue bars) and Re = 100 (red bars) at Pe = $[10^2, 10^3, 10^4]$. (b) Percentage change in reaction amount between Re = 100 and Re = 1 $((\mathrm{Nc}_{@\mathrm{Re}=100} - \mathrm{Nc}_{@\mathrm{Re}=1})/Nc_{@Re=1})$ for three Pe values.

2. *Reaction Dynamics*

To further quantify the effects of inertia and diffusion on reactive transport dynamics, we characterize the bulk fluid–solid reaction dynamics using the global (effective) reaction rate, R_C, defined as the time derivative of the C particle accumulation, N_C, as defined as follows [63]:

$$R_C = \frac{dN_C}{dt}. \tag{9}$$

Fig. 6 shows the time evolution of the global reaction rate for combinations of Re = [1, 100] and Pe = $[10^2, 10^3, 10^4]$. Fig. 6 (a) shows the results for two cases wherein the ratio of Pe to Re is fixed to 100, whereas Figs. 6 (b–d) show the results for Re = 1 and Re = 100 at three different Pe. Fig. 6 (a) can be understood as showing two cases wherein the solute–solvent combinations are fixed, but the injection rates differ by two orders of magnitude. On the other hand, Figs. 6 (b–d) help to discern the respective effects of Re and Pe on the global reaction rate. The results show that the early reaction regime is controlled mainly by Pe, whereas the later regime is more sensitive to Re. Specifically, for the same Pe, Re = 1 and Re = 100 result in similar initial global reaction rates, and increasing the Pe significantly decreases the initial global reaction rates (see the y-intercepts in Figs. 6 (b–d)).

The facilitation of fluid–solid reactions by the increase in fluid inertia (Re) is evident in the later stages of the reactive transport: the increase in Re significantly enhances the reaction duration, and this effect intensifies as Pe increases. This is because the recirculating flows increase the residence time via the trapping effect, which enhances reaction. Because the trapping effect increases as Pe increases, the enhanced reaction rate and the prolonged reaction duration at Re = 100 become more evident as Pe increases. The reaction enhancement by the increase in Re is consistent with the result in Fig. 5 (b).

The results have direct implications on the well-known discrepancy between effective reaction rates measured under fluid flow conditions and the reaction rates measured under well-mixed conditions [3, 14, 31, 92–99]. For fluid–solid reactions, the effective reaction rates depend on the reactant concentrations near the fracture surfaces, and flow structures and diffusion affect spatiotemporal distribution of reactants [28, 29, 100]. The estimated global reaction rates highlight the effects of fluid inertia and solute diffusion on the effective reaction rates.

The time evolution of the total number of C particles further highlights the inertia and diffusion effects on fluid–solid reaction dynamics. As shown in Fig. 7, fluid inertia increases the generation rate of C particles, as shown by the slopes. Specifically, the slopes are consistently larger at Re = 100 than at Re = 1, and the difference between these two cases increases as Pe increases. This is because of the flow channeling and trapping effects by recirculation zones; the flow channeling increases overall spreading of the particles and once the A particles are trapped, they are more likely to react with the walls because the diffusion effect becomes dominant in the recirculation zones. Fig. 7 confirms that recirculation zones facilitate the fluid–solid reaction, and that such effect intensifies as Pe increases. Note that the magnitude of the slope is more sensitive to Pe than to Re, which is consistent with the results shown in Fig. 6.

Fig. 7 also shows that fluid inertia increases the reaction duration, which is defined as the time interval between the first and last reactions. The differences in reaction duration between Re = 1 and Re = 100 are denoted by ΔT (Figs. 7 (a–c)). The increased reaction duration at Re = 100 shows that the recirculating flows increase not only the global reaction rate but also the reaction duration. To directly estimate the role of recirculating flows on the reactive transport dynamics, we estimated the percentage of the reactions that occurred in recirculation zones during ΔT and during the entire reaction duration for Re = 100. Fig. 7 (d) shows that the percentage is consistently larger during the ΔT period (red lines) than in the entire reaction duration (blue lines). Furthermore, the percentage increases as Pe increases. This indicates that the recirculation zones play a more dominant role in the fluid–solid reaction at high Pe regimes and at later times. The result confirms that the recirculating flows are the main cause of the prolonged reaction duration.

To elucidate the relation between transport and reaction dynamics, we now quantify the reaction frequency as a function of Lagrangian velocity magnitudes. First, for each particle trajectory, we estimate average Lagrangian velocity magnitudes at every $\Delta x = a$. In other words, we estimate the average Lagrangian velocity whenever a particle travels a longitudinal distance of a. Subsequently, we sample the velocity values for the injected A particles up to the point when they undergo reactions and the velocities at which the A particles underwent reactions. From this information, we count the total frequency of each velocity class from all sampled velocities (All in Fig. 8) and also from the velocities at which the A particles underwent reactions (Reac in Fig. 8). Note that we discretized the velocity magnitudes into 100 classes (bins) that are equally spaced in log scale.

Fig. 8 highlights the importance of the underlying flow fields on heterogeneous reactions. First, small velocity magnitudes ($< 10^0$) exhibit significantly higher frequencies at Re = 100 than at Re = 1. This is because the recirculating flows that develop at Re = 100 significantly enhance the frequencies of small velocities. Second, the solid (velocity frequencies for A particles) and dashed (velocity frequencies at reaction locations) lines are almost identical at small velocity magnitudes ($< 10^0$) but exhibit a large discrepancy at larger velocity magnitudes ($> 10^0$). This result indicates that the A particles are highly likely to undergo reactions at small velocities, but not at high velocities. Lastly, particles experience broader velocity ranges at Re = 100 than at Re = 1. In the following section, we use the understanding of reaction dynamics that we have established thus far to upscale the reactive transport.

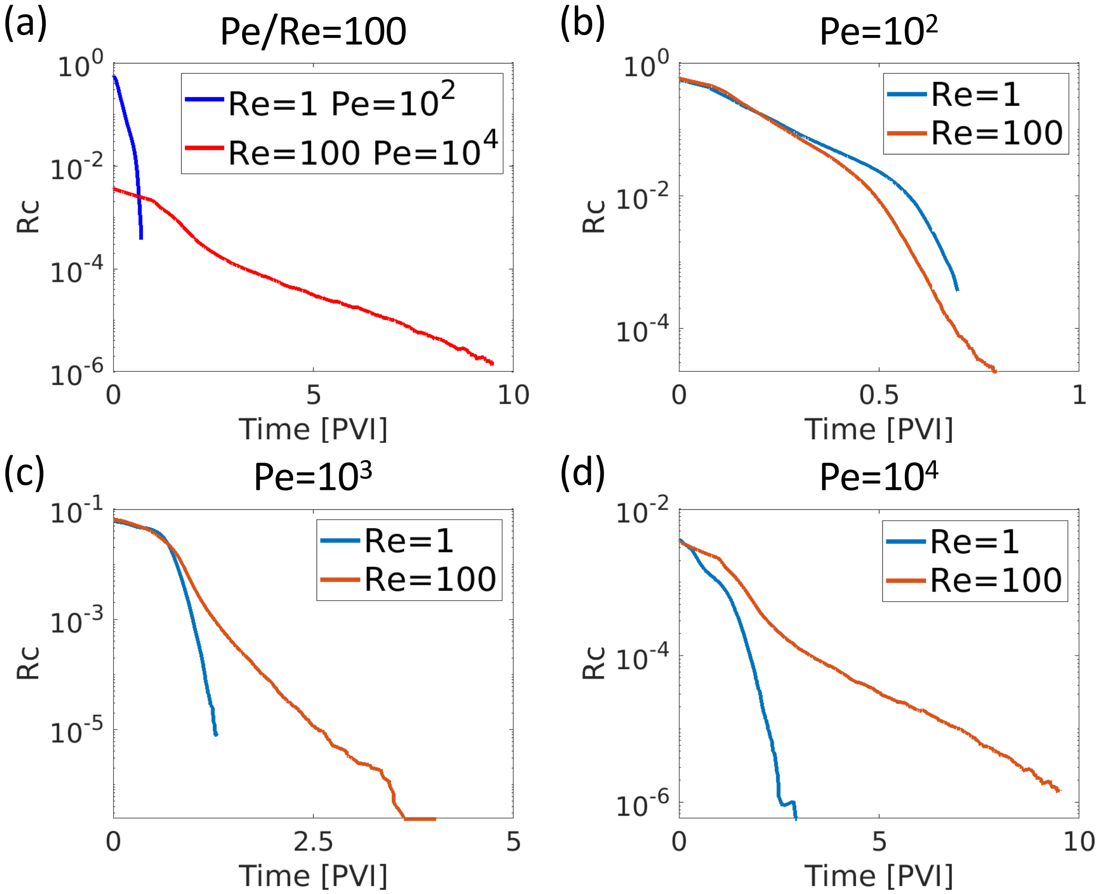

FIG. 6. (a) Time evolution of global reaction rate (R_C) at Re = 1 & Pe = 10^2 (solid blue line) and Re = 100 & Pe = 10^3 (solid red line). Global reaction rates (R_C) at Re = 1 (solid sky-blue lines) and Re = 100 (solid orange lines) for (b) Pe = 10^2, (c) Pe = 10^3, and (d) Pe = 10^4. Time is normalized by one pore volume injection (1 PVI).

IV. UPSCALED MODEL FOR REACTIVE TRANSPORT WITH FLUID–SOLID REACTIONS

In this section, we present the development of a parsimonious upscaled model that effectively captures reactive transport. The upscaled model helps identify the key factors controlling the fluid-solid reactive transport dynamics. It can also effectively capture the key reactive transport processes without substantial computational resources. The computation time is 40 to 800 times faster, depending on the Re and Pe combination, for the upscaled model. Note that the computation time depends on the number of particles used in the upscaled model and this comparison assumes that the parameters for the upscaled model are known. In recent years, upscaled models based on continuous-time random walk (CTRW) theory have been successfully applied to both conservative [38, 39, 58, 101–110] and reactive transport in heterogenous media [46, 48, 49, 58, 62, 87, 110–113]. However, it is currently unclear how to upscale reactive transport with surface reactions over wide ranges of inertia and diffusion regimes in rough fracture flows. Here, we extend the Spatial Markov model (SMM), a type of CTRW that explicitly honors velocity correlation [104]. We extend the SMM by incorporating a reaction probability model that is parameterized with Lagrangian velocities.

A. Lagrangian Velocity Statistics

We first characterize the Lagrangian velocity statistics which are the key input parameters to the SMM. We discretize the particle trajectories as successive jumps of a fixed distance $\Delta x = a$ in the longitudinal direction (mean flow direction):

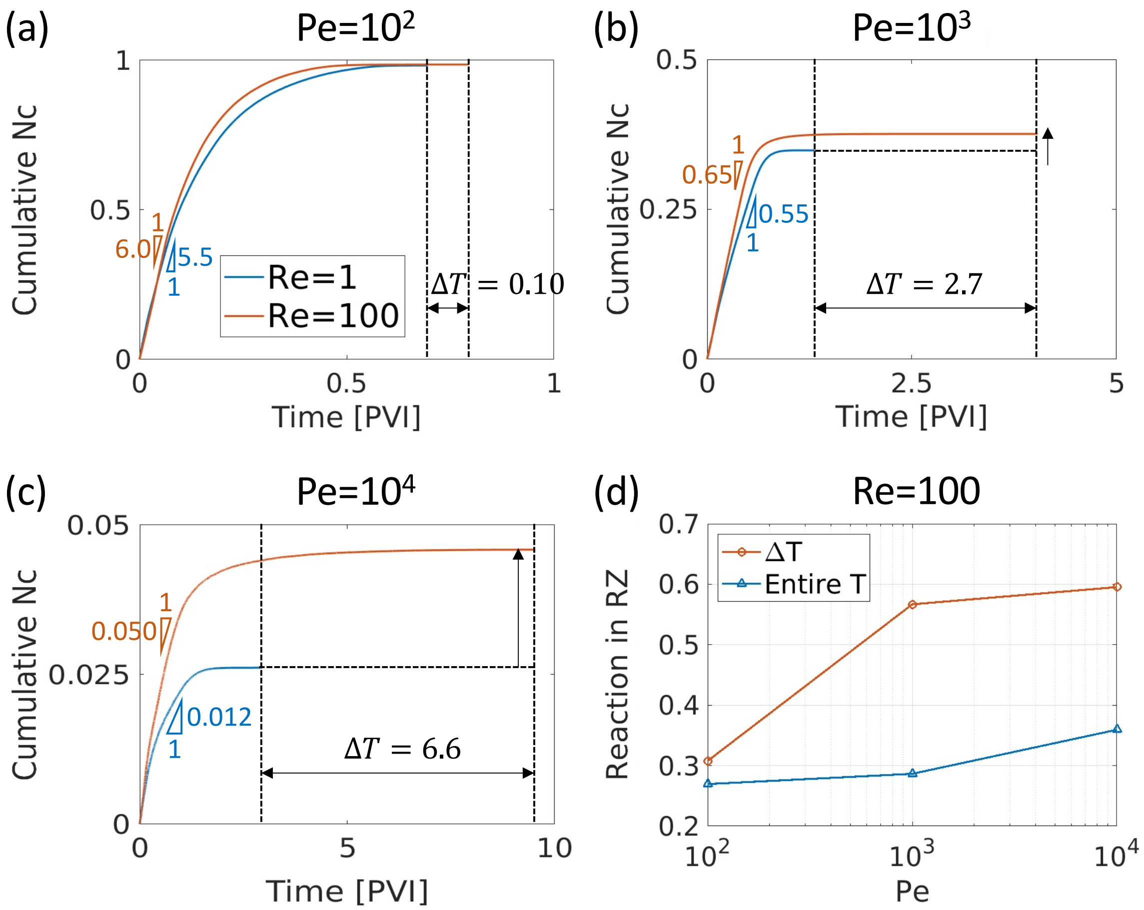

FIG. 7. Number of product C particles normalized based on total number of injected particles at Re $=1$ (solid blue lines) and Re $=100$ (solid orange lines) for (a) Pe $=10^2$, (b) Pe $=10^3$, and (c) Pe $=10^4$. Each line represents the average of ten realizations, and time is normalized based on one pore volume injection (1 PVI). (d) Percentage of reactions that occurred in recirculation zones (RZ) in ΔT (blue solid line with circles) and for the entire time (Entire T, orange solid line with triangles) at Re $=100$ as function of Pe.

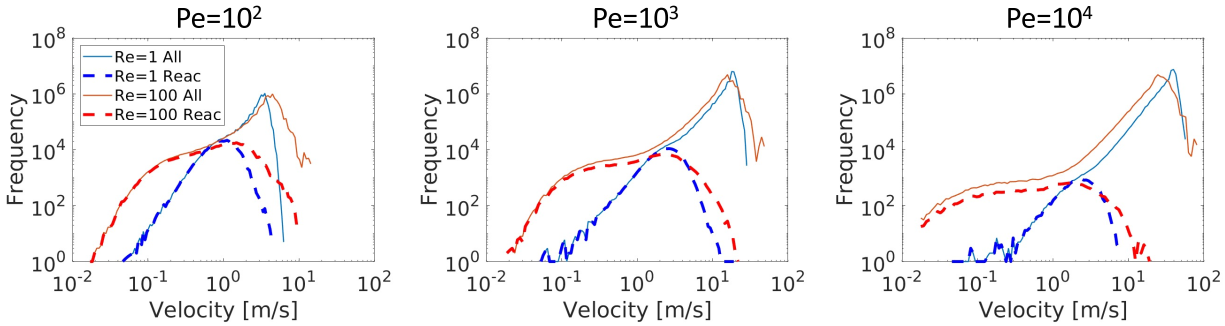

FIG. 8. Frequencies of sampled velocities up to point when particles undergo reactions (solid blue lines for Re $=1$ and solid orange lines for Re $=100$) and sampled velocities at which reactions occurred (blue dashed lines for Re $=1$ and red dashed lines for Re $=100$) at Pe $=[10^2, 10^3, 10^4]$.

$$x^{(n+1)} = x^{(n)} + \Delta x, \quad t^{(n+1)} = t^{(n)} + \tau^{(n)}, \tag{10}$$

where $x^{(n)}$ and $t^{(n)}$ are the particle location and time at a jump step n, and $\tau^{(n)}$ is the transition time. The transition time is related to the Lagrangian velocity $v^{(n)}$ as $\tau^{(n)} = \frac{\Delta x}{v^{(n)}}$. For each Re-Pe combination, we sampled the Lagrangian velocities $v^{(n)}$ from all particle trajectories of 10 ensembles.

Lagrangian velocity statistics can be effectively characterized by velocity transition matrices, as shown in Fig. 9 (a). To construct the velocity transition matrices, the Lagrangian velocities, $v^{(n)} = \frac{\Delta x}{\tau^{(n)}}$, are classified into the 100 velocity classes, $i = [1, ..., 100]$, which are evenly spaced in log scale. Note that $i = 1$ and $i = 100$ are the slowest and fastest velocity classes, respectively. The velocity transition matrices show the velocity transition probability (T_{ij}) between the current i and next j velocity classes. The value of T_{ij} indicates the probability of sampling the j-th velocity class given the i-th velocity class.

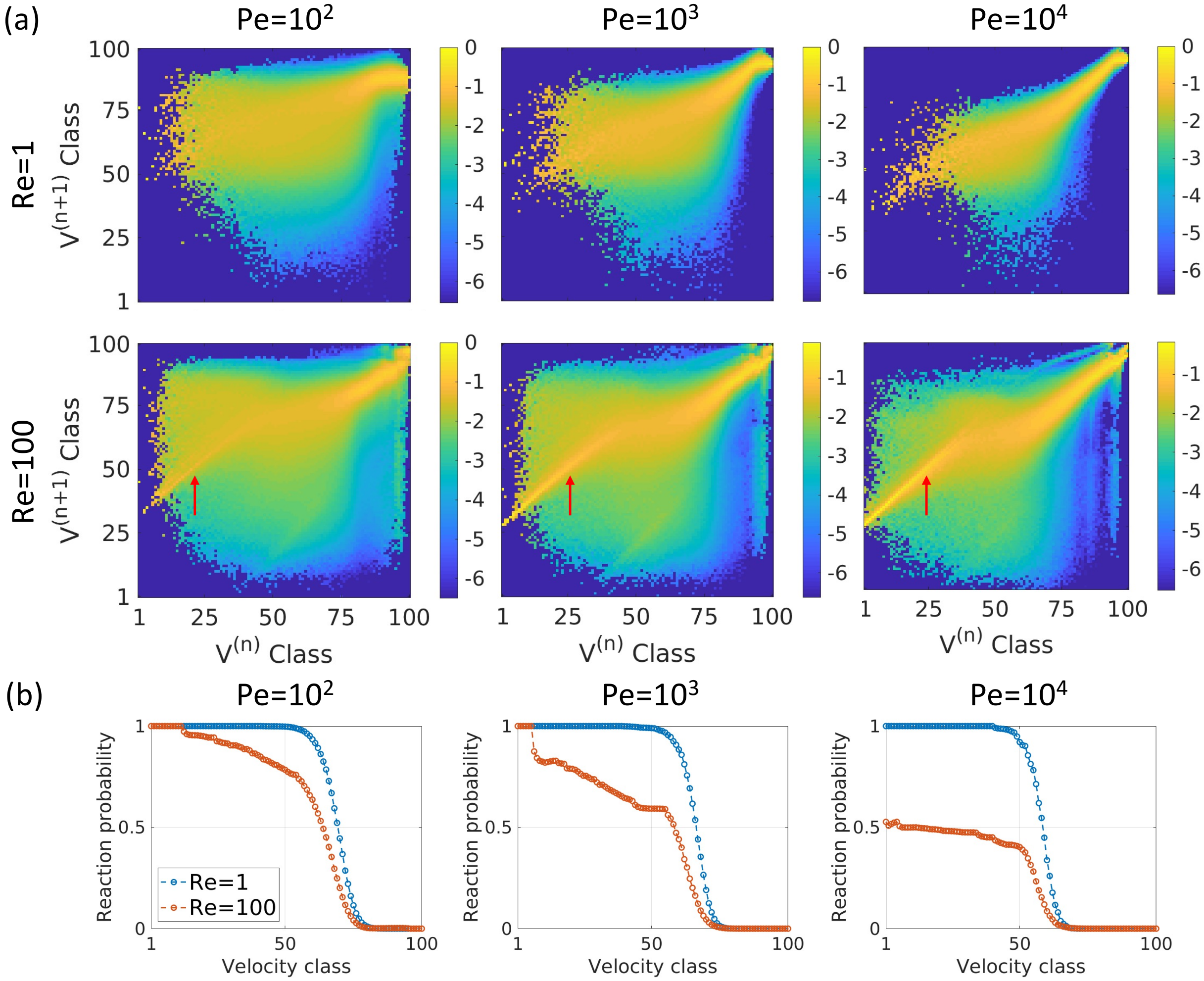

FIG. 9. (a) Velocity transition matrices for combinations of Re = [1, 100] and Pe = $[10^2, 10^3, 10^4]$. (b) Velocity-dependent ($P_{\mathrm{rxn}|i}$) reaction probabilities as function of velocity classes for Re = 1 (dashed blue lines with circle marks) and 100 (dashed red lines with circle marks) at Pe = $[10^2, 10^3, 10^4]$. Note that velocity class 1 is the slowest velocity class, and 100 is the fastest velocity class.

The transition matrices effectively capture the effects of both flow channeling and recirculating flows on transport. First, the diagonal elements of the transition matrices tend to have larger values compared to the off-diagonal elements, especially for high-velocity regimes ($75 \leq i \leq 100$). Higher probabilities along the diagonal elements imply the tendency to maintain one's velocity. Thus, the diagonal values are large when the velocity correlation is large which is the case for high-velocity regimes: the particles in the main flow channel are likely to continue to experience fast velocities. Furthermore, the probability along the diagonal elements increases as Re increases, which can be explained by the enhancement of flow channeling due to the recirculating flows developed at Re = 100 (Fig. 2 (b)). The probability along the diagonal elements also increases as Pe increases because particles tend to stay in a streamline at high Pe regimes.

Velocity correlation decreases as velocity magnitude decreases, especially for Re = 1, but an interesting phenomenon arises at Re = 100. The particles with low velocities tend to transit to higher velocities, as indicated by the red arrows in Fig. 9 (a). This is because the trapped particles in recirculating flows tend to experience high velocities in the main channel flow when they exit the recirculation zones. A similar phenomenon was recently reported for solute transport in turbulent channel flows over porous media [114].

Lastly, we compute the velocity-dependent reaction probabilities. We first obtain N_i and $N_{\mathrm{rxn},i}$, where N_i is the total frequency of the sampled i-th velocity class that A particles experience until reaction, and $N_{\mathrm{rxn},i}$ is the total frequency of the sampled i-th velocity class at which reaction occurs. We then calculate the velocity-dependent reaction probability at each i-th velocity class, $P_{[\mathrm{rxn}|i]}$, by dividing $N_{\mathrm{rxn},i}$ by N_i as follows:

$$P_{[\mathrm{rxn}|i]} = \frac{N_{\mathrm{rxn},i}}{N_i},\ i = [1, ..., 100]. \tag{11}$$

Fig. 9 (b) shows the velocity-dependent reaction probabilities for all combinations of Re = [1, 100] and Pe = $[10^2, 10^3, 10^4]$. The figure shows that the reaction probabilities decrease as velocity magnitude increases. This is because the fluid–solid reaction is more likely to occur at small velocities. At Re = 100, the reaction probability decreases as Pe increases because the particles become less likely to react due to low diffusivity. However, recirculation zones still enhance the overall reaction amount because the recirculation zones significantly enhance the frequencies of experiencing small velocities (as shown in Fig. 8), which have higher reaction probabilities than those at high velocities. In particular, the red solid lines and red dashed lines in Figs. 8 (a) and (b) (Re = 100 & Pe = 10^2 and Re = 100 & 10^3 cases) almost overlap at small velocities. This means that the reaction probability at the small velocities, which occurs mostly inside recirculating flows, is almost one, as illustrated in the first and second panels (Pe = 10^2 and 10^3 cases) of Fig. 9 (b). However, for the Re = 100 and Pe = 10^4 case, the strong advection prevents particles to react even at small velocity regions and therefore the reaction probability decreases significantly.

B. Upscaled Model Predictions

Here, we extend the SMM framework by incorporating a reaction step with the velocity-dependent reaction probability (Eq. (11)) as follows:

$$x^{(n+1)} = x^{(n)} + \Delta x, \quad t^{(n+1)} = t^{(n)} + \tau^{(n)}, \quad p = \begin{cases} A, & \text{otherwise} \\ C, & \text{if } P_{[\mathrm{rxn}|i^{(n)}]} \geq \xi \end{cases}, \tag{12}$$

where $i^{(n)}$ is the velocity class at the n-th step, p is the particle type (A or C), and ξ is a sampled random variable from a uniform distribution between 0 and 1. The transport and reaction steps sequentially iterate as follows. At the n-th step, an A particle moves Δx, and the transition time $\tau^{(n)}$ is determined based on the previous transition time $\tau^{(n-1)}$ and the transition matrix (Fig. 9 (a)). The A particle then converts to a C particle if the velocity-dependent reaction probability at the velocity class $i^{(n)}$, $P_{[\mathrm{rxn}|i^{(n)}]}$, is larger than the sampled value ξ. The transport and reaction steps continue sequentially. Once an A particle converts to a C particle, it remains as a C particle, and undergoes only the transport step. We refer to the SMM framework coupled with the reaction step as reactive SMM.

Fig. 10 shows the FPTDs of the A and C particles from the direct numerical simulations (DNS) and the reactive SMM predictions for combinations of Re = [1, 100] and Pe = $[10^2, 10^3, 10^4]$ at the two breakthrough locations (x = [$20a$, $90a$]). Fig. 10 (b) shows the FPTDs of A particles that survived until they reached the breakthrough locations. The reactive SMM accurately captures the FPTDs of both A and C particles in all Re and Pe cases at both locations (x = [$20a$, $90a$]). The good performance of the model indicates that the effects of inertia and diffusion on the reactive transport with fluid–solid reactions can be effectively described by the reactive SMM.

To elucidate the importance of honoring the velocity-dependent reaction probability for the reactive transport predictions, we also perform upscaled modeling with an average reaction probability. We derive the average (velocity-independent) reaction probability from the concept of the survival probability $P_{\mathrm{sur}} = (1 - P_{\mathrm{rxn}})^{N_{\mathrm{jump}}}$, i.e., the probability of the A particles to not undergo reactions while they take N_{jump} steps along the x-direction (mean flow direction). Note that N_{jump} is determined as a quotient of the longitudinal travel distance and Δx. The average reaction probability can be expressed with the survival probability, as follows:

$$P_{\mathrm{rxn}} = 1 - P_{\mathrm{sur}}^{\frac{1}{N_{\mathrm{jump}}}}, \quad \text{where } P_{\mathrm{sur}} = 1 - \frac{N_C}{N_{\mathrm{inj}}}, \tag{13}$$

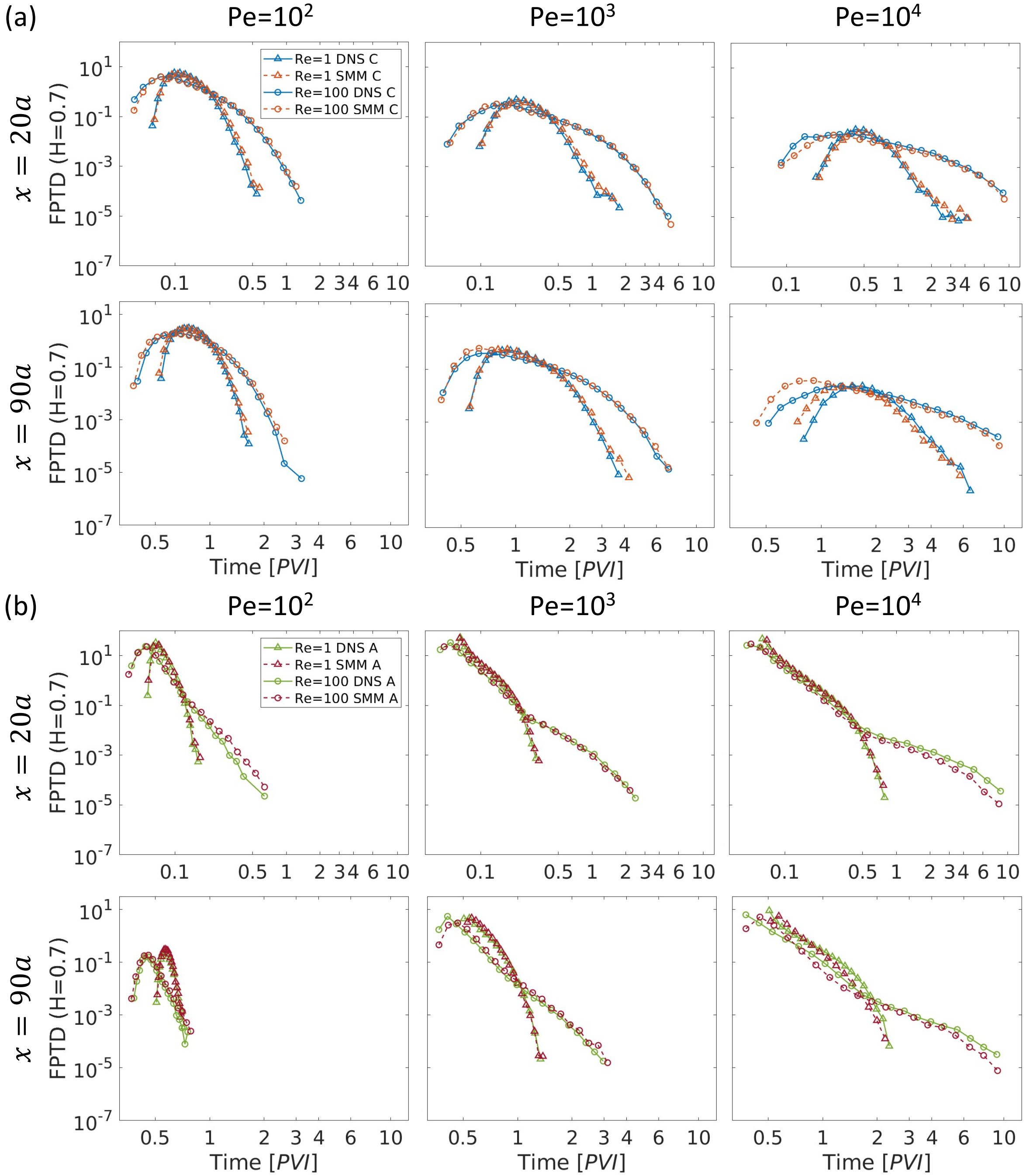

FIG. 10. (a) FPTDs of C particles from direct numerical simulations (DNS) (solid blue lines) and FPTDs from reactive SMM predictions (dashed orange lines) at $x = [20a,\ 90a]$. (b) FPTDs of A particles from direct numerical simulations (DNS) (solid green lines) and FPTDs from reactive SMM predictions (dashed brown lines) at $x = [20a,\ 90a]$.

where N_C is the total number of the product C particles, and N_{inj} is the total number of injected A particles. The velocity-independent reaction probabilities for all combinations of $\mathrm{Re} = [1,\ 100]$ and $\mathrm{Pe} = [10^2, 10^3, 10^4]$ are shown in Table 1. Note that the average reaction probability honors the total reaction amount but does not account for the velocity-dependence of reaction probability.

Fig. 11 shows the FPTDs of the C particles from DNS and from SMM predictions with the average reaction probability, P_{rxn}, for combinations of $\mathrm{Re} = [1,\ 100]$ and $\mathrm{Pe} = [10^2, 10^3, 10^4]$ at both locations ($x = [20a,\ 90a]$). At $\mathrm{Pe} = 100$, the SMM with the average reaction probability still reasonably captures the FPTDs because the velocity

P_{rxn}	$\mathrm{Pe} = 10^2$	$\mathrm{Pe} = 10^3$	$\mathrm{Pe} = 10^4$
$\mathrm{Re} = 1$	0.050	0.0054	0.00034
$\mathrm{Re} = 100$	0.052	0.0059	0.00059

TABLE I. Average reaction probabilities for combinations of $\mathrm{Re} = [1,\ 100]$ and $\mathrm{Pe} = [10^2, 10^3, 10^4]$.

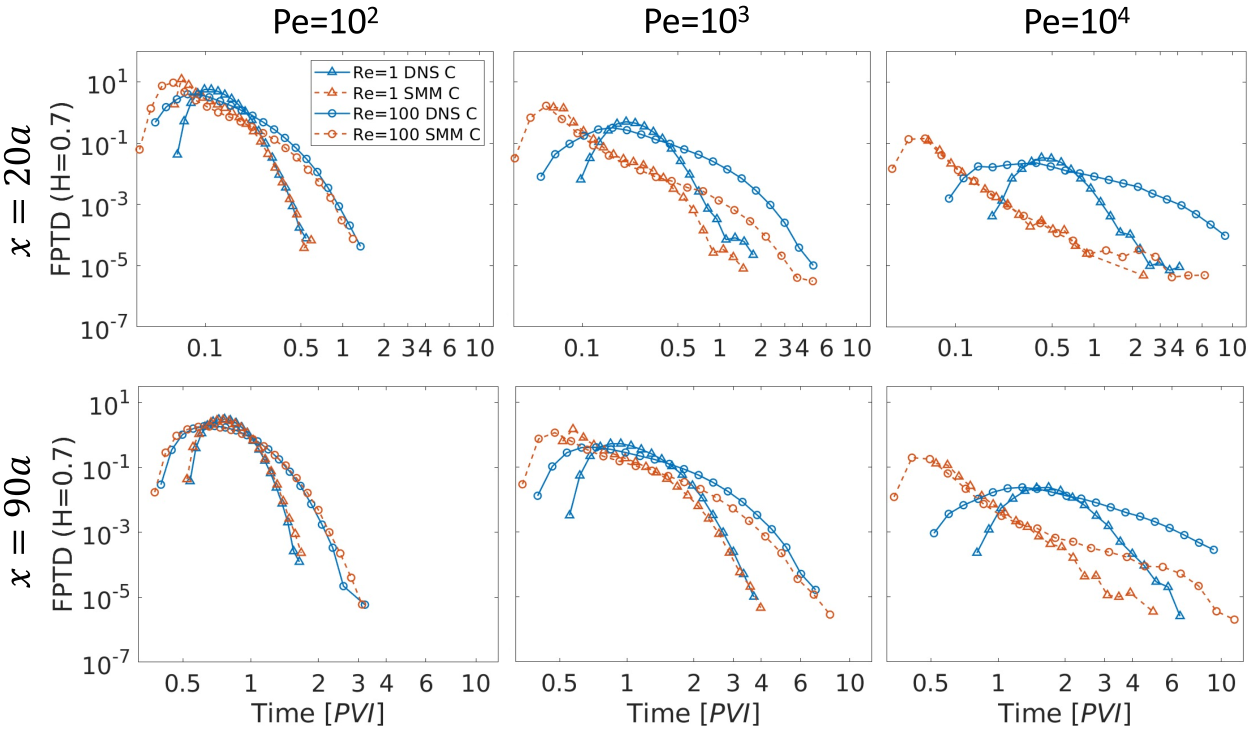

FIG. 11. FPTDs of C particles from direct numerical simulations (DNS) (solid blue lines) and from model predictions (dashed orange lines) with the average reaction probability at $x = [20a,\ 90a]$.

correlation is weak when diffusion is strong. However, the accuracy significantly deteriorates as Pe increases (at both locations of $x = [20a,\ 90a]$). When the advective transport is strong, the particle movements become sensitive to the flow properties, and thus the fluid–solid reactions are strongly affected by the flow properties. Therefore, as Pe increases, the model with the average reaction probability results in poor predictability because the model does not honor the flow effects on the reaction probability. This result confirms that transport and reaction dynamics are intimately coupled, and that both transport and reaction dynamics can be well captured by reactive SMM but not by models that do not honor the velocity-dependent reaction probability. Note that the upscaled model is validated with the diffusion-limited catalytic reaction system only. So, further study is necessary to verify the model's capability for other reaction systems.

V. CONCLUSIONS

In this study, we investigated the effects of fluid inertia and solute diffusion on reactive transport involving fluid–solid reactions in rough fracture flows. To focus on the Re and Pe effects on reactive transport, we considered an irreversible and instantaneous fluid–solid reaction, $A + Solid \rightarrow C$, using the Lagrangian-based reactive particle tracking method. We improved the fundamental understanding of inertia and diffusion effects on reactive transport and, consequently, successfully upscaled the reactive transport.

Both fluid inertia and solute diffusion are shown to control the fluid–solid reactive transport dynamics. Solute diffusion (Pe) controls mainly the total reaction amount, whereas fluid inertia (Re) governs the reaction dynamics by inducing complex flow structures such as flow channeling and recirculating flows. Flow channeling, featured by fast velocities and high-velocity correlation, limits fluid–solid reactions. For example, in high-Pe regimes, the particles in the flow channeling region tend to stay in the fast flow channel, which limits surface reactions. By contrast, in low-Pe regimes, the injected particles can easily traverse the fracture width via diffusion, lowering the prominence of the flow channeling effect.

Recirculating flows are shown to significantly affect surface reactions via the trapping effect. The recirculation zones exhibit slow velocities and are advectively separated from the main flow channels. Once particles enter these recirculation zones, the trapped particles stay for a long time near the fracture surfaces, which increases reaction probability. Our study explicitly showed that these recirculating flows can significantly facilitate surface reactions and increase reaction duration via the trapping effect for the transport-limited reaction considered in this study. Further, we showed that such inertia and diffusion effects on fluid–solid reactions can be effectively captured by the velocity-dependent reaction probability.

Based on this improved understanding of the fluid–solid reaction dynamics in rough fracture flows, we successfully upscaled the reactive transport in rough fracture flows by incorporating the velocity-dependent reaction probability into the Spatial Markov model. The proposed reactive SMM accurately captured the transport of both the reactant and product particles. The good performance of the proposed reactive SMM demonstrates that reactive transport in fracture flows can be effectively upscaled using Lagrangian velocity statistics and the velocity-dependent reaction rule. The proposed upscaled model could be incorporated into a network-scale model such that one can accurately incorporate the effects of fracture-scale processes in network-scale reactive transport.

ACKNOWLEDGMENTS

The authors thank the Minnesota Supercomputing Institute (MSI) at the University of Minnesota for computational resources. The authors also acknowledge grants from the National Science Foundation (NSF) via Grant No. EAR1813526 and the Korea Environment Industry & Technology Institute (KEITI) through Subsurface Environment Management (SEM) Project (2020002440002) funded by the Korea Ministry of Environment (MOE). P. K. K. acknowledges the College of Science and Engineering at the University of Minnesota and the George and Orpha Gibson Endowment.

[1] A. Hartmann, N. Goldscheider, T. Wagener, J. Lange, and M. Weiler, Karst water resources in a changing world: Review of hydrological modeling approaches, Rev. Geophys. **52**, 218 (2014).
[2] B. Berkowitz, Characterizing flow and transport in fractured geological media: A review, Phys. Rev. Lett. **25**, 861 (2002).
[3] K. T. MacQuarrieand K. U. Mayer, Reactive transport modeling in fractured rock: A state-of-the-science review, Earth-Sci. Rev. **72**, 189 (2005).
[4] J. Bear, C.-F. Tsang, and G. De Marsily, *Flow and contaminant transport in fractured rock* (Academic Press, Inc, 1993).
[5] L. Morenoand I. Neretnieks, Fluid flow and solute transport in a network of channels, J. Contam. Hydrol. **14**, 163 (1993).
[6] G. S. Bodvarsson, W. Boyle, R. Patterson, and D. Williams, Overview of scientific investigations at yucca mountain—the potential repository for high-level nuclear waste, J. Contam. Hydrol. **38**, 3 (1999).
[7] K. Pruess, Enhanced geothermal systems (EGS) using CO2 as working fluid—a novel approach for generating renewable energy with simultaneous sequestration of carbon, Geothermics **35**, 351 (2006).
[8] H. Yasuhara, A. Polak, Y. Mitani, A. S. Grader, P. M. Halleck, and D. Elsworth, Evolution of fracture permeability through fluid–rock reaction under hydrothermal conditions, Earth Planet. Sci. Lett. **244**, 186 (2006).
[9] F. Gabrovšekand W. Dreybrodt, Karstification in unconfined limestone aquifers by mixing of phreatic water with surface water from a local input: a model, J. Hydrol. **386**, 130 (2010).
[10] L. De Windt, A. Burnol, P. Montarnal, and J. van der Lee, Intercomparison of reactive transport models applied to UO2 oxidative dissolution and uranium migration, J. Contam. Hydrol. **61**, 303 (2003).
[11] N. Spycher, E. Sonnenthal, and J. Apps, Fluid flow and reactive transport around potential nuclear waste emplacement tunnels at yucca mountain, nevada, J. Contam. Hydrol. **62**, 653 (2003).
[12] K. Pedersen, Microbial life in deep granitic rock, FEMS Microbiol. Rev. **20**, 399 (1997).
[13] K. Pedersen, Exploration of deep intraterrestrial microbial life: current perspectives, FEMS Microbiol. Rev. **185**, 9 (2000).
[14] C. I. Steefel, D. J. DePaolo, and P. C. Lichtner, Reactive transport modeling: An essential tool and a new research approach for the earth sciences, Earth Planet. Sci. Lett. **240**, 539 (2005).
[15] Y.-S. Jun, D. E. Giammar, and C. J. Werth, Impacts of geochemical reactions on geologic carbon sequestration, Environ. Sci. Technol **47**, 3 (2013).
[16] A. Aubeneau, B. Hanrahan, D. Bolster, and J. L. Tank, Substrate size and heterogeneity control anomalous transport in small streams, Geophys. Res. Lett. **41**, 8335 (2014).
[17] M. W. Losey, R. J. Jackman, S. L. Firebaugh, M. A. Schmidt, and K. F. Jensen, Design and fabrication of microfluidic devices for multiphase mixing and reaction, J Microelectromech Syst **11**, 709 (2002).

[18] A. J. Demello, Control and detection of chemical reactions in microfluidic systems, Nature **442**, 394 (2006).

[19] B. Kwon, L. Liebenberg, A. M. Jacobi, and W. P. King, Heat transfer enhancement of internal laminar flows using additively manufactured static mixers, Int J Heat Mass Transf **137**, 292 (2019).

[20] R. Liu, S. Yao, Y. Li, and J. Cheng, Pore-scale study of dynamic ion adsorption process in porous electrodes of capacitive deionization using lattice boltzmann method, Int. J. Heat Mass Transf. **135**, 769 (2019).

[21] O. Iliev, Z. Lakdawala, K. H. Neßler, T. Prill, Y. Vutov, Y. Yang, and J. Yao, On the pore-scale modeling and simulation of reactive transport in 3d geometries, Math. Model. Anal. **22**, 671 (2017).

[22] M. Liu, J. Waugh, S. K. Babu, J. S. Spendelow, and Q. Kang, Numerical modeling of ion transport and adsorption in porous media: A pore-scale study for capacitive deionization desalination, Desalination **526**, 115520 (2022).

[23] V. M. Calo, O. Iliev, Z. Lakdawala, K. Leonard, and G. Printsypar, Pore-scale modeling and simulation of flow, transport, and adsorptive or osmotic effects in membranes: The influence of membrane microstructure, Int J Adv Eng Sci Appl Math. **7**, 2 (2015).

[24] E. Kjeang, R. Michel, D. A. Harrington, N. Djilali, and D. Sinton, A microfluidic fuel cell with flow-through porous electrodes, J Am Chem Soc **130**, 4000 (2008).

[25] W. Pan, P. Wang, X. Chen, F. Wang, and G. Dai, Combined effects of flow channel configuration and operating conditions on pem fuel cell performance, Energy Convers Manag **220**, 113046 (2020).

[26] N. Mladenov, J. Koop, S. Tischer, and O. Deutschmann, Modeling of transport and chemistry in channel flows of automotive catalytic converters, Chemical Engineering Science **65**, 812 (2010).

[27] O. Deutschmann, Modeling of the interactions between catalytic surfaces and gas-phase, Catalysis Letters **145**, 272 (2015).

[28] C. I. Steefeland K. Maher, Fluid-rock interaction: A reactive transport approach, Rev. Mineral. Geochem. **70**, 485 (2009).

[29] H. Dengand N. Spycher, Modeling reactive transport processes in fractures, Rev. Mineral. Geochem. **85**, 49 (2019).

[30] H. Deng, S. Molins, D. Trebotich, C. Steefel, and D. DePaolo, Pore-scale numerical investigation of the impacts of surface roughness: Upscaling of reaction rates in rough fractures, Geochim. Cosmochim. Acta **239**, 374 (2018).

[31] K. Maherand A. Navarre-Sitchler, Reactive transport processes that drive chemical weathering: From making space for water to dismantling continents, Rev. Mineral. Geochem. **85**, 349 (2019).

[32] S. Yoon, M. Dentz, and P. K. Kang, Optimal fluid stretching for mixing-limited reactions in rough channel flows, J. Fluid Mech. **916** (2021).

[33] D. F. Boutt, G. Grasselli, J. T. Fredrich, B. K. Cook, and J. R. Williams, Trapping zones: The effect of fracture roughness on the directional anisotropy of fluid flow and colloid transport in a single fracture, Geophys. Res. Lett. **33** (2006).

[34] M. B. Cardenas, D. T. Slottke, R. A. Ketcham, and J. M. Sharp Jr, Navier-stokes flow and transport simulations using real fractures shows heavy tailing due to eddies, Geophys. Res. Lett. **34** (2007).

[35] S. H. Lee, I. W. Yeo, K.-K. Lee, and R. L. Detwiler, Tail shortening with developing eddies in a rough-walled rock fracture, Geophys. Res. Lett. **42**, 6340 (2015).

[36] Z. Dou, Z. Chen, Z. Zhou, J. Wang, and Y. Huang, Influence of eddies on conservative solute transport through a 2d single self-affine fracture, Int. J. Heat Mass Transf. **121**, 597 (2018).

[37] J. S. Kim, I. W. Seo, D. Baek, and P. K. Kang, Recirculating flow-induced anomalous transport in meandering open-channel flows, Ad Water Res **141**, 103603 (2020).

[38] S. Yoonand P. K. Kang, Roughness, inertia, and diffusion effects on anomalous transport in rough channel flows, Phys. Rev. Fluids **6**, 014502 (2021).

[39] P. K. Kang, T. Le Borgne, M. Dentz, O. Bour, and R. Juanes, Impact of velocity correlation and distribution on transport in fractured media: Field evidence and theoretical model, Water Resources Research **51**, 940 (2015).

[40] P. K. Kang, S. Brown, and R. Juanes, Emergence of anomalous transport in stressed rough fractures, Earth Planet. Sci. Lett. **454**, 46 (2016).

[41] T. Sherman, N. B. Engdahl, G. Porta, and D. Bolster, A review of spatial markov models for predicting pre-asymptotic and anomalous transport in porous and fractured media, J. contam. hydrol. , 103734 (2020).

[42] D. Bolster, K. R. Roche, and V. L. Morales, Recent advances in anomalous transport models for predicting contaminants in natural groundwater systems, Curr. Opin. Chem. Eng. **26**, 72 (2019).

[43] M. C. Richmond, W. A. Perkins, T. D. Scheibe, A. Lambert, and B. D. Wood, Flow and axial dispersion in a sinusoidal-walled tube: Effects of inertial and unsteady flows, Adv. Water Resour. **62**, 215 (2013).

[44] B. D. Wood, Inertial effects in dispersion in porous media, Water resources research **43** (2007).

[45] S. H. Leeand P. K. Kang, Three-dimensional vortex-induced reaction hot spots at flow intersections, Phys. Rev. Lett. **124**, 144501 (2020).

[46] S. Yoonand P. K. Kang, Mixing-induced bimolecular reactive transport in rough channel flows: Pore-scale simulation and stochastic upscaling, Transp. Porous Media , 1 (2021).

[47] C.-X. Zhou, R. Hu, H.-W. Li, Z. Yang, and Y.-F. Chen, Pore-scale visualization and quantification of dissolution in microfluidic rough channels, Water Resour. Res. **58**, e2022WR032255 (2022).

[48] N. L. Sund, D. Bolster, and C. Dawson, Upscaling transport of a reacting solute through a peridocially converging–diverging channel at pre-asymptotic times, J. contam. hydrol. **182**, 1 (2015).

[49] T. Sherman, A. Paster, G. Porta, and D. Bolster, A spatial markov model for upscaling transport of adsorbing-desorbing solutes, J. contam. hydrol. **222**, 31 (2019).

[50] B. B. Mandelbrot, *The fractal geometry of nature* (WH freeman New York, 1983).

[51] J. Kertesz, V. K. Horvath, and F. Weber, Self-affine rupture lines in paper sheets, Fractals **1**, 67 (1993).

[52] L. Ponson, D. Bonamy, and E. Bouchaud, Two-dimensional scaling properties of experimental fracture surfaces, Phys. Rev. Lett. **96**, 035506 (2006).

[53] E. Bouchaud, G. Lapasset, and J. Planes, Fractal dimension of fractured surfaces: a universal value?, EPL **13**, 73 (1990).

[54] G. Drazer, H. Auradou, J. Koplik, and J. Hulin, Self-affine fronts in self-affine fractures: Large and small-scale structure, Phys. Rev. Lett. **92**, 014501 (2004).

[55] R. F. Voss, Fractals in nature: from characterization to simulation, in *The science of fractal images* (Springer, 1988) pp. 21–70.

[56] H.-H. Liu, G. S. Bodvarsson, S. Lu, and F. J. Molz, A corrected and generalized successive random additions algorithm for simulating fractional levy motions, Math. Geosci. **36**, 361 (2004).

[57] OpenFOAM, The open source cfd toolbox, http://wwwopenfoamcom (2011).

[58] D. Bolster, Y. Méheust, T. Le Borgne, J. Bouquain, and P. Davy, Modeling preasymptotic transport in flows with significant inertial and trapping effects–the importance of velocity correlations and a spatial markov model, Adv. Water Resour. **70**, 89 (2014).

[59] A. D. Stroock, S. K. Dertinger, A. Ajdari, I. Mezić, H. A. Stone, and G. M. Whitesides, Chaotic mixer for microchannels, Science **295**, 647 (2002).

[60] J. Delgado, A critical review of dispersion in packed beds, Heat Mass Transf. **42**, 279 (2006).

[61] J. Delgadoand J. G. de Carvalho, Measurement of the coefficient of transverse dispersion in flow through packed beds for a wide range of values of the schmidt number, Transp porous media **44**, 165 (2001).

[62] T. Aquinoand T. Le Borgne, The chemical continuous time random walk framework for upscaling transport limitations in fluid–solid reactions, Adv. Water Resour. **154**, 103981 (2021).

[63] A. Nissanand B. Berkowitz, Reactive transport in heterogeneous porous media under different peclet numbers, Water Resour. Res. **55**, 10119 (2019).

[64] L. J. Perez, J. J. Hidalgo, and M. Dentz, Upscaling of mixing-limited bimolecular chemical reactions in poiseuille flow, Water Resour. Res. **55**, 249 (2019).

[65] S. Ó. Snæbjörnsdóttir, B. Sigfússon, C. Marieni, D. Goldberg, S. R. Gislason, and E. H. Oelkers, Carbon dioxide storage through mineral carbonation, Nat. Rev. Earth Environ. **1**, 90 (2020).

[66] A. Raza, G. Glatz, R. Gholami, M. Mahmoud, and S. Alafnan, Carbon mineralization and geological storage of co2 in basalt: Mechanisms and technical challenges, Earth Sci Rev **229**, 104036 (2022).

[67] D. T. Gillespie, The chemical langevin equation, J. Chem. Phys. **113**, 297 (2000).

[68] M. Liu, M. Shabaninejad, and P. Mostaghimi, Impact of mineralogical heterogeneity on reactive transport modelling, Comput. Geosci. **104**, 12 (2017).

[69] R. L. Detwiler, R. J. Glass, and W. L. Bourcier, Experimental observations of fracture dissolution: The role of peclet number on evolving aperture variability, Geophys. Res. Lett. **30** (2003).

[70] R. L. Detwilerand H. Rajaram, Predicting dissolution patterns in variable aperture fractures: Evaluation of an enhanced depth-averaged computational model, Water Resour. Res. **43** (2007).

[71] R. Garg, S. Nair, and A. N. Bhaskarwar, Mass transfer with instantaneous chemical reaction in finite gas–liquid systems, Chem. Eng. Technol. **76**, 89 (2000).

[72] N. Batensand R. Van Keer, On a numerical relaxation method for a chemical reaction-diffusion problem with an instantaneous and irreversible reaction, Chem. Eng. Sci. **58**, 4815 (2003).

[73] M. Khanand M. Van Swaay, Non-equilibrium theory of capillary columns and the effect of interfacial resistance on column efficiency, Gas Chromatography (ed. M. Van Swaay) , 3 (1962).

[74] L. Zhang, M. A. Hesse, and M. Wang, Transient solute transport with sorption in poiseuille flow, J. Fluid Mech. **828**, 733 (2017).

[75] M. v. Smoluchowski, Versuch einer mathematischen theorie der koagulationskinetik kolloider lösungen, Zeitschrift für physikalische Chemie **92**, 129 (1918).

[76] S. A. Rice, *Diffusion-limited reactions* (Elsevier, 1985).

[77] H. Van Beijeren, W. Dong, and L. Bocquet, Diffusion-controlled reactions: A revisit of noyes' theory, J Chem Phys **114**, 6265 (2001).

[78] E. Kotominand V. Kuzovkov, *Modern aspects of diffusion-controlled reactions: Cooperative phenomena in bimolecular processes* (Elsevier, 1996).

[79] G. H. Weiss, Overview of theoretical models for reaction rates, J. Stat. Phys. **42**, 3 (1986).

[80] A. Szabo, Theory of diffusion-influenced fluorescence quenching, J Phys Chem **93**, 6929 (1989).

[81] B. Bijeljic, P. Mostaghimi, and M. J. Blunt, Signature of non-fickian solute transport in complex heterogeneous porous media, Phys. Rev. Lett. **107**, 204502 (2011).

[82] P. Mostaghimi, B. Bijeljic, M. Blunt, *et al.*, Simulation of flow and dispersion on pore-space images, SPE J. **17**, 1 (2012).

[83] J. P. Nunes, B. Bijeljic, and M. Blunt, Time-of-flight distributions and breakthrough curves in heterogeneous porous media using a pore-scale streamline tracing algorithm, Transp Porous Media **109**, 317 (2015).

[84] H. Risken, Fokker-planck equation, in *The Fokker-Planck Equation* (Springer, 1996) pp. 63–95.

[85] M. J. Schmidt, S. D. Pankavich, and D. A. Benson, On the accuracy of simulating mixing by random-walk particle-based mass-transfer algorithms, Adv. Water Resour. **117**, 115 (2018).

[86] M. J. Schmidt, N. B. Engdahl, D. A. Benson, and D. Bolster, Optimal time step length for lagrangian interacting-particle simulations of diffusive mixing, Transp. Porous Media **146**, 413 (2023).

[87] N. L. Sund, G. M. Porta, and D. Bolster, Upscaling of dilution and mixing using a trajectory based spatial markov random walk model in a periodic flow domain, Adv. Water Resour. **103**, 76 (2017).

[88] See supplemental material at [url will be inserted by publisher] for movies showing reactive transport simulation results

at Re = 1 & Pe = 10^3 and Re = 100 & Pe = 10^3.

[89] J.-Q. Zhou, L. Wang, Y.-F. Chen, and M. B. Cardenas, Mass transfer between recirculation and main flow zones: Is physically based parameterization possible?, Water Resour. Res. **55**, 345 (2019).

[90] M. B. Cardenas, D. T. Slottke, R. A. Ketcham, and J. M. Sharp Jr, Effects of inertia and directionality on flow and transport in a rough asymmetric fracture, J. Geophys. Res. Solid Earth **114** (2009).

[91] J. Bouquain, Y. Méheust, D. Bolster, and P. Davy, The impact of inertial effects on solute dispersion in a channel with periodically varying aperture, Phys. Fluids **24**, 083602 (2012).

[92] L. Li, C. I. Steefel, and L. Yang, Scale dependence of mineral dissolution rates within single pores and fractures, Geochim. Cosmochim. Acta **72**, 360 (2008).

[93] C. Soulaine, S. Pavuluri, F. Claret, and C. Tournassat, porousmedia4foam: Multi-scale open-source platform for hydro-geochemical simulations with openfoam, Earth and Space Science Open Archive ESSOAr (2021).

[94] J. D. Rimstidtand P. M. Dove, Mineral/solution reaction rates in a mixed flow reactor: Wollastonite hydrolysis, Geochim. Cosmochim. Acta **50**, 2509 (1986).

[95] M. A. Williamsonand J. D. Rimstidt, The kinetics and electrochemical rate-determining step of aqueous pyrite oxidation, Geochim. Cosmochim. Acta **58**, 5443 (1994).

[96] C. M. Gramling, C. F. Harvey, and L. C. Meigs, Reactive transport in porous media: A comparison of model prediction with laboratory visualization, Environ. Sci. Technol **36**, 2508 (2002).

[97] D. S. Rajeand V. Kapoor, Experimental study of bimolecular reaction kinetics in porous media, Environ. Sci. Technol **34**, 1234 (2000).

[98] C. Knutson, A. Valocchi, and C. Werth, Comparison of continuum and pore-scale models of nutrient biodegradation under transverse mixing conditions, Adv. Water Resour. **30**, 1421 (2007).

[99] P. K. Kang, E. Bresciani, S. An, and S. Lee, Potential impact of pore-scale incomplete mixing on biodegradation in aquifers: From batch experiment to field-scale modeling, Adv. Water Resour. **123**, 1 (2019).

[100] M. Liu, B. Kwon, and P. K. Kang, Machine learning to predict effective reaction rates in 3d porous media from pore structural features, Scientific Reports **12**, 1 (2022).

[101] N. B. Engdahland D. Bolster, Markovian transport processes in a heterogeneous, variably saturated watershed: A multi-domain spatial markov model, Adv Water Resour **138**, 103555 (2020).

[102] N. B. Engdahland T. Aquino, Upscaled models for time-varying solute transport: Transient spatial-markov dynamics, Adv Water Resour **166**, 104271 (2022).

[103] B. Berkowitz, A. Cortis, M. Dentz, and H. Scher, Modeling non-fickian transport in geological formations as a continuous time random walk, Rev. Geophys. **44** (2006).

[104] T. Le Borgne, M. Dentz, and J. Carrera, Spatial markov processes for modeling lagrangian particle dynamics in heterogeneous porous media, Phys. Rev. E **78**, 026308 (2008).

[105] T. Le Borgne, M. Dentz, and J. Carrera, Lagrangian statistical model for transport in highly heterogeneous velocity fields, Phys. Rev. Lett. **101**, 090601 (2008).

[106] P. K. Kang, M. Dentz, T. Le Borgne, and R. Juanes, Spatial markov model of anomalous transport through random lattice networks, Phys. Rev. Lett. **107**, 180602 (2011).

[107] P. K. Kang, P. De Anna, J. P. Nunes, B. Bijeljic, M. J. Blunt, and R. Juanes, Pore-scale intermittent velocity structure underpinning anomalous transport through 3-d porous media, Geophys. Res. Lett. **41**, 6184 (2014).

[108] M. Dentz, P. K. Kang, A. Comolli, T. Le Borgne, and D. R. Lester, Continuous time random walks for the evolution of lagrangian velocities, Phys. Rev. Fluids **1**, 074004 (2016).

[109] V. L. Morales, M. Dentz, M. Willmann, and M. Holzner, Stochastic dynamics of intermittent pore-scale particle motion in three-dimensional porous media: Experiments and theory, Geophys. Res. Lett. **44**, 9361 (2017).

[110] T. Sherman, E. B. Janetti, G. R. Guédon, G. Porta, and D. Bolster, Upscaling transport of a sorbing solute in disordered non periodic porous domains, Adv. Water Resour. **139**, 103574 (2020).

[111] T. Aquinoand M. Dentz, Chemical continuous time random walks, Phys. Rev. Lett. **119**, 230601 (2017).

[112] T. Aquinoand M. Dentz, Kinetics of contact processes under segregation, Phys. Rev. E. **101**, 012114 (2020).

[113] A. Massoudiehand M. Dentz, Upscaling non-linear reactive transport in correlated velocity fields, Adv. Water Resour. **143**, 103680 (2020).

[114] J. S. Kim, P. K. Kang, S. He, L. Shen, S. S. Kumar, J. Hong, and I. W. Seo, Pore-scale flow effects on solute transport in turbulent channel flows over porous media, Transp Porous Media , 1 (2022).